Volume 16
Number 2
14 January 2024
Pages 491-944

Nanoscale

rsc.li/nanoscale

ISSN 2040-3372

ROYAL SOCIETY OF CHEMISTRY

PAPER
Milad Abolhasani *et al.*
Autonomous nanomanufacturing of lead-free metal halide perovskite nanocrystals using a self-driving fluidic lab

NCNST

Nanoscale

PAPER

View Article Online
View Journal | View Issue

Cite this: *Nanoscale*, 2024, **16**, 580

Autonomous nanomanufacturing of lead-free metal halide perovskite nanocrystals using a self-driving fluidic lab†

Sina Sadeghi,[a] Fazel Bateni,[a] Taekhoon Kim,[b] Dae Yong Son,[b] Jeffrey A. Bennett,[a] Negin Orouji,[a] Venkat S. Punati,[a] Christine Stark,[a] Teagan D. Cerra,[c] Rami Awad,[a] Fernando Delgado-Licona,[a] Jinge Xu,[a] Nikolai Mukhin,[a] Hannah Dickerson,[a] Kristofer G. Reyes[d] and Milad Abolhasani *[a]

Lead-based metal halide perovskite (MHP) nanocrystals (NCs) have emerged as a promising class of semiconducting nanomaterials for a wide range of optoelectronic and photoelectronic applications. However, the intrinsic lead toxicity of MHP NCs has significantly hampered their large-scale device applications. Copper-base MHP NCs with composition-tunable optical properties have emerged as a prominent lead-free MHP NC candidate. However, comprehensive synthesis space exploration, development, and synthesis science studies of copper-based MHP NCs have been limited by the manual nature of flask-based synthesis and characterization methods. In this study, we present an autonomous approach for the development of lead-free MHP NCs *via* seamless integration of a modular microfluidic platform with machine learning-assisted NC synthesis modeling and experiment selection to establish a self-driving fluidic lab for accelerated NC synthesis science studies. For the first time, a successful and reproducible in-flow synthesis of $Cs_3Cu_2I_5$ NCs is presented. Autonomous experimentation is then employed for rapid in-flow synthesis science studies of $Cs_3Cu_2I_5$ NCs. The autonomously generated experimental NC synthesis dataset is then utilized for fast-tracked synthetic route optimization of high-performing $Cs_3Cu_2I_5$ NCs.

Received 6th October 2023,
Accepted 7th December 2023

DOI: 10.1039/d3nr05034c

rsc.li/nanoscale

1. Introduction

Lead (Pb)-based metal halide perovskite (MHP) nanocrystals (NCs) have been of great interest in the field of photonic and optoelectronic devices due to their intriguing size- and composition-tunable properties, excellent color purity, high photoluminescence quantum yield (PLQY), large absorption cross section, and facile solution-phase synthesis and processing.[1–9] Despite the excellent optical attributes of Pb-based MHP NCs, their large-scale adoption by photonic devices is greatly hampered by Pb toxicity and stability challenges against light, moisture, heat, and electric field. To tackle Pb toxicity, there have been multiple recent efforts to replace either the Pb^{2+} ion with a nontoxic divalent ion (*e.g.*, Sn^{2+} and Ge^{2+}),[10–14] or two divalent Pb^{2+} ions with a pair of one monovalent ion (*e.g.*, Ag^{+}) and one trivalent ion (*e.g.*, Bi^{3+}, Sb^{3+}, and In^{3+}) used to form double-perovskite NCs.[15–18] However, stability issues of Sn^{2+} and Ge^{2+} ions under ambient conditions as well as relatively low PLQY and indirect bandgap of double-perovskite NCs still hinder their device applications.

Low-dimensional MHP NCs possess interesting optical features, such as a wide bandgap energy and a large Stokes shift, attributed to the isolation of coordinated metal octahedra by surrounding cations.[19] This phenomenon results in the self-trapped exciton (STE) emission mechanism, that is originated from the lattice deformation of MHP structure.[20–24] All-inorganic copper (Cu)-based MHP NCs, $Cs_3Cu_2X_5$ (X: Cl, Br, I), have recently emerged as a promising Pb-free MHP candidate due to their low toxicity and earth-abundant elements.[19,25,26] In one example, Lu *et al.* studied the effects of reaction time and temperature on the morphology of $Cs_3Cu_2Cl_5$ NCs and found that increasing the reaction temperature results in the formation of nanorods.[26] Among different Cu-based MHP NCs, $Cs_3Cu_2I_5$ exhibits a high stability under ambient condition. $Cs_3Cu_2I_5$ NCs have a pure orthorhombic crystal structure, where tetrahedral [CuI_4] and trigonal [CuI_3] units are

[a]*Department of Chemical and Biomolecular Engineering, North Carolina State University, Raleigh, NC 27695, USA. E-mail: abolhasani@ncsu.edu*
[b]*Synthesis Technical Unit, Material Research Center, Samsung Advanced Institute of Technology, SEC, 130, Samsung-ro, Yeongtong-gu, Suwon-si, Gyeonggi-do, Republic of Korea*
[c]*Department of Physics, Weber State University, Ogden, UT 84408, USA*
[d]*Department of Materials Design and Innovation, University at Buffalo, Buffalo, NY 14260, USA*

† Electronic supplementary information (ESI) available. See DOI: https://doi.org/10.1039/d3nr05034c

edge-shared to form $[Cu_2I_5]$ clusters that are isolated by cesium (Cs) cations.[19] The recent successful colloidal synthesis of Cu-based MHP NCs[19,25,26] warrants further understanding of their vast synthesis-property relationship toward on-demand scalable production.

Prior studies of Cu-based MHP NCs have utilized conventional batch reactors for the NC synthesis and screening *via* the hot-injection (HI) synthetic technique.[19,25,26] In spite of the facile control and operation of batch reactors, the fast formation kinetics of ionic MHP NCs could result in reproducibility issues in batch reactors stemming from the mass transfer-dependent precursor conversion rates. Additionally, limited accessibility of batch processes to *in situ* characterization techniques along with their irreproducible mass and heat transfer rates further complicate the fundamental and applied studies of Cu-based MHP NCs.[4,27–29] In addition, the high-dimensional reaction space of Pb-free MHP NCs, arising from various precursors, ligands, reaction time, and temperature, brings significant challenges while searching for optimal NC synthesis condition required to achieve desired optical properties. Compared to batch reactors, droplet-based microfluidic synthesis strategies have been demonstrated as a reliable reactor of choice for high-throughput screening, mechanistic studies, and continuous production of colloidal NCs, including metal oxide, silver, and gold NCs, as well as II–VI, III–V, and Pb-based MHP NCs.[30–39]

The continuous nature of microfluidic reactors along with their modularity, facile automation, and integration with multimodal *in situ* characterization tools (*e.g.*, spectroscopy)[28,40,41] offer an exciting avenue to accelerate parameter space and synthesis-property relationship mapping of NCs through integration with data science tools in a closed-loop format. Such integration of an automated microfluidic reactor with machine learning (ML)-assisted process modelling and experiment-selection results in establishment of self-driving fluidic labs (SDFLs).[42–44] Autonomous experimentation enabled by SDFLs automates the loop of hypothesis generation, planning and choosing the next set of experiments, performing selected experiments, and analyzing new experimental outcomes to refine/reject/validate the hypothesis.[45–50] Furthermore, reaction miniaturization, modularity, and automation of microfluidic reactors significantly enhance the quality and quantity of the experimental data (low experimental noise) required to train the ML predictive models of SDFLs while minimizing chemical consumption. A variety of ML techniques, including Bayesian optimization (BO) which resolves uncertainty and reinforcement learning have been adopted by SDFLs to intelligently navigate the vast synthesis space of NCs.[51–56,66] Fig. 1 illustrates the advantages of SDFLs over conventional flow chemistry platforms.

Herein, we report a SDFL for accelerated synthesis-parameter relationship mapping and autonomous nanomanufacturing of Pb-free MHP NCs. Specifically, we focus on autonomous synthesis of $Cs_3Cu_2I_5$ NCs, as an emerging Pb-free MHP testbed. First, utilizing the automation mode of the developed flow chemistry platform, we investigate the effects of synthetic parameters, including precursors concentration, ligands population, reaction time, and temperature, on the optical properties of the in-flow synthesized $Cs_3Cu_2I_5$ NCs. Next, we demonstrate the importance of ML model tuning and uncertainty quantification on the total cost of autonomous NC synthesis experimental campaigns. Then, we utilize the developed SDFL for accelerated parameter space mapping, optimization, and autonomous nanomanufacturing of high-performing $Cs_3Cu_2I_5$ NCs with minimum experimental cost.

Milad Abolhasani

Milad Abolhasani is an Associate Professor, ALCOA Scholar, and a University Faculty Scholar in the Department of Chemical and Biomolecular Engineering at North Carolina State University. He received his Ph.D. from the University of Toronto in 2014. Prior to joining NC State University in 2016, he was an NSERC Postdoctoral Fellow in the Department of Chemical Engineering at MIT. At NC State University, Dr. Abolhasani leads a flow chemistry research group that studies self-driving labs tailored toward accelerated discovery, development, and manufacturing of advanced functional materials and molecules using autonomous experimentation.

2. Experimental

2.1 Chemicals

Oleic acid (OA, 90%), oleylamine (OAm, 70%), copper (I) iodide (CuI, 99.999% trace metal basis, M_w = 190.45 g mol^{-1}), and hexane (70%) were purchased from Sigma-Aldrich. 1-Octadecene (ODE, 90%) and cesium carbonate (Cs_2CO_3, 99.9% metal basis, M_w = 325.82 g mol^{-1}) were purchased from Fisher Scientific. High-performance heat transfer perfluorinated oil (PFO) was purchased from Solvay. All chemicals were used without further purification.

2.2 Precursor preparation

We adapted the HI precursor chemistry reported by Li *et al.* using a coupled metal and halide precursor with minor modifications to achieve completely soluble Cs-oleate and CuI precursors at room temperature and successful reproducible synthesis of $Cs_3Cu_2I_5$ NCs in flow.[25] In order to prevent precipitation in the setup precursor delivery module and achieve highly consistent results, a Cs : OA molar ratio of at least 1 : 5 should be used while preparing the initial Cs-oleate precursor to obtain a full conversion of the Cs salt. The 1 : 5 molar ratio not only results in a soluble Cs-oleate precursor at room temperature that benefits flow synthesis of NCs, but also improves reproducibility of the Cs-oleate-based MHP NC syntheses.[57] In

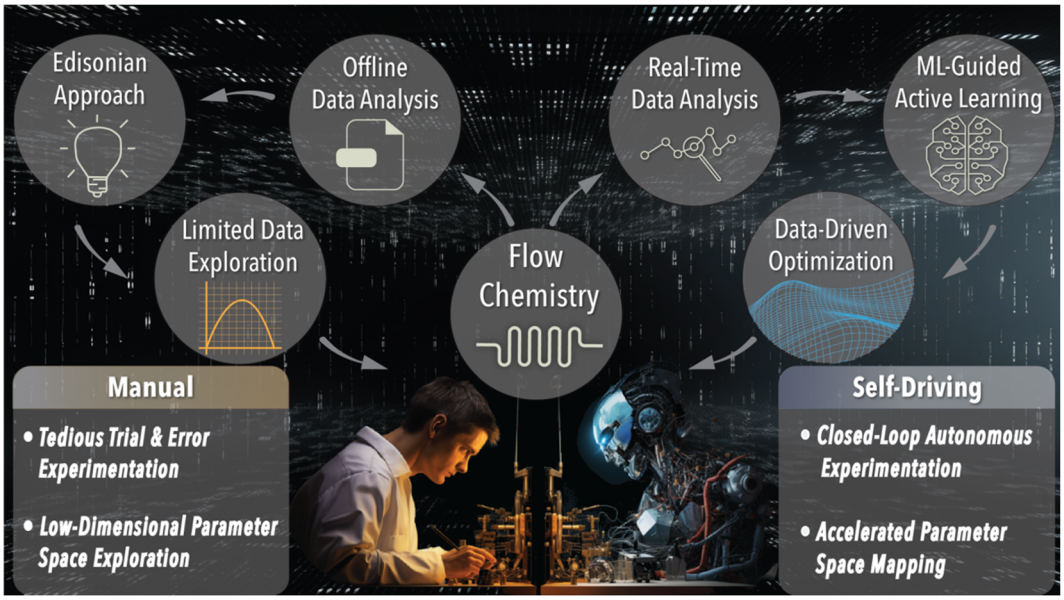

Fig. 1 Conventional flow chemistry *vs.* a SDFL for accelerated development and optimization of colloidal NCs.

the most reported HI MHP NC synthesis chemistries to synthesize $Cs_3Cu_2X_5$ (X: Cl, Br, I) NCs, the Cs-oleate precursor is insoluble when cooled to room temperature. Therefore, we modified the HI precursor chemistry reported by Li *et al.* and developed a new protocol for preparation of stock precursor solutions (Cs-oleate and CuI) amenable to flow synthesis. The new precursor chemistry resulted in completely soluble Cs-oleate and CuI precursors at room temperature and successful reproducible in-flow synthesis of $Cs_3Cu_2I_5$ NCs.

2.3.1 Cs-oleate precursor. 240 mg Cs_2CO_3, 3.75 mL OA, and 45 mL ODE were loaded into a 100 mL 3-neck flask which was then maintained under vacuum for 1 h at 120 °C. The mixture was subsequently heated under N_2 to 150 °C and maintained at this temperature for 30 min to ensure a complete conversion of the Cs salt.

2.3.2 CuI precursor. 0.45 mmol CuI, 5 mL OA, 5 mL OAm, and 50 mL ODE were loaded into a 100 mL 3-neck flask and maintained under vacuum for 1 h at 120 °C. The solution was subsequently purged with N_2 at 120 °C for 30 min.

2.3.3 Ligands. The concentrated stock solutions of the NC ligands, including two OA-ODE and one OAm-ODE solutions were prepared using a 1 : 4 ligand : ODE volumetric ratio.

All stock solutions were loaded into the gas-tight stainless-steel syringes (50 mL, Chemyx) under inert conditions after reaching room temperature.

2.3 Experimental setup

Fig. 2 illustrates the schematic of the developed flow chemistry platform for autonomous synthesis and development of Pb-free MHP NCs (see Fig. S1† for an image of the experimental setup). The automated flow chemistry platform is comprised of three distinct modules: fluid delivery, mixing and reaction, and *in situ* characterization. In the fluid delivery module, seven syringe pumps equipped with gas-tight stainless-steel syringes (50 mL) were utilized to precisely deliver a desired concentration of the stock solutions at a specific volumetric flowrate to the mixing junctions used to form the precursor streams. The mixed Cs-oleate and CuI streams were then guided to the reaction module where the NC synthesis happens. In order to separate the reactive phase containing the NC precursors from the flow reactor walls during the NC synthesis, an inert carrier phase, PFO, was utilized to form a lubrication film around the reactive phase and obtain a two-phase liquid–liquid segmented flow format (see ESI Movie M1†). The carrier phase (PFO) was continuously delivered to the flow segmentation junction (Fig. 2) using a computer-controlled syringe pump equipped with a gas-tight stainless-steel syringe (100 mL). The material-efficient nature of the developed flow chemistry platform allows for accelerated exploration of up to 100 different experimental conditions of Pb-free MHP NCs per batch of stock solutions while using only a total of 1 mL NC precursors per experimental condition.

The fluid delivery module includes eight computer-controlled syringe pumps (Chemyx Fusion 6000) loaded with seven 50 mL and one 100 mL gas-tight stainless-steel syringes (Chemyx) for precursors and PFO, respectively. The precursor formulation and reaction module includes a custom-designed reactor heating plate and three fluidic connections used for the formation of the CuI, Cs-oleate, and reaction streams.

CuI precursor stream with a desired concentration and ligand ratio was formed by the in-flow mixing of the stock solution of CuI precursor with three streams of OA-ODE (1 : 4 volumetric ratio), OAm-ODE (1 : 4 volumetric ratio), and solvent (ODE) in a five-way fluidic connection (IDEX). The Cs-oleate stream was formed by the in-flow mixing of the Cs-oleate precursor with OA-ODE (1 : 4 volumetric ratio) and solvent (ODE)

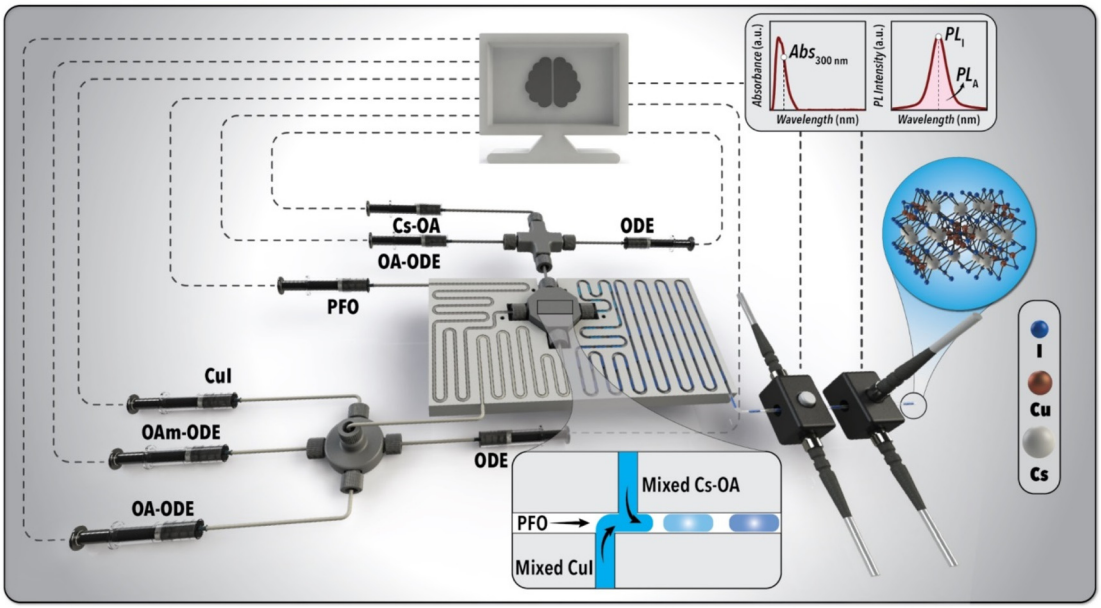

Fig. 2 Schematic illustration of the developed SDFL for fast-tracked synthesis and development of Pb-free MHP NCs.

in a four-way fluidic connection (IDEX). All precursor streams were connected to the fluidic connections using a fluorinated ethylene propylene (FEP) tubing (1/16″ outer diameter, OD × 0.02″ inner diameter, ID). The formulated CuI and Cs-oleate precursors with the desired concentrations (adjusted *via* aforementioned in-flow mixing process) as well as the inert carrier fluid (PFO) were delivered to a custom-designed four-way fluidic connection (PEEK) using perfluroalkoxy (PFA) tubing (1/16″ OD × 0.02″ ID) to form a liquid–liquid two-phase segmented flow. PFA was specifically selected for the preheating and the synthesis modules of the flow chemistry platform because of its high temperature stability (melting temperature of 310 °C). Two in-line static micromixers (*i.e.*, braided tubing) were utilized to ensure uniform mixing of the CuI and Cs-oleate streams before entering the flow segmentation module. The CuI and PFO streams were placed inside the custom-designed heating plate (aluminium) to preheat to the desired reaction temperature, while Cs-oleate was directed to the segmentation module at room temperature. The heating plate was heated using three cartridge heaters (Watlow) and a PID temperature controller (F4T, Watlow) to obtain desired synthesis temperature both for the preheated precursors and the NC synthesis module. In order to rapidly characterize the optical properties of the in-flow synthesized Pb-free MHP NCs, the reactor outlet was given enough length to cool down to the room temperature before being connected to the *in situ* characterization module. In order to increase the light pathlength for spectroscopy within the flowcell, a larger ID tubing (FEP tubing, 1/16″ OD × 0.04″ ID) than the flow reactor module (PFA, 1/16″ OD × 0.03″ ID) was used for spectroscopy. Due to different light intensity and slit requirements for the *in situ* photoluminescence (PL) and absorption spectral characterizations of Pb-free MHP NCs, two flowcells with two fiber-coupled spectrometers were utilized for real-time monitoring of the optical properties of the in-flow synthesized Pb-free MHP NCs. The first flowcell was connected to a 300 nm UV LED (Thorlabs) and a miniature spectrometer (Ocean Insight HDX, 200 μm slit) in a 90° configuration for PL spectroscopy. The second flowcell was connected to a broadband light source (Ocean Insight, DH-2000-BAL) and another miniature spectrometer (Ocean Insight HDX, 5 μm slit) in a 180° configuration for absorption spectroscopy.

3. Results and discussion

The in-flow NC synthesis followed a HI synthetic approach where the CuI and PFO streams were preheated to the desired reaction temperature ranging from 120 °C to 150 °C while Cs-oleate was directed to the flow segmentation junction at room temperature. The liquid–liquid segmented flow was obtained by combining the reactive phase stream (NC precursors) and PFO at the segmentation module. The NC synthesis time in the flow reactor was varied by changing the total volumetric flowrate of the NC precursors. The developed flow chemistry platform could automatically perform up to 100 experimental conditions using a single batch of precursor solutions. Seven independent input parameters, including reaction temperature and volumetric flowrates of CuI, Cs-oleate, two OA-ODE streams, OAm-ODE, and solvent (ODE) associated with the CuI stream, were controlled for automated synthesis of Pb-free MHP NCs. Next, the range of residence (reaction) times resulting in Pb-free MHP NCs in the flow reactor was identified by varying the precursors volumetric flowrates. The solvent (ODE) volumetric flowrate of the Cs-oleate stream was automatically adjusted to accommodate the 1 : 1 volumetric injection ratio

for mixed precursor streams. In addition, the carrier phase (PFO) volumetric flowrate was automatically adjusted with respect to the total volumetric flowrate of both precursor streams. The 1 : 1 injection ratio of precursor streams as well as the PFO volumetric flowrate equalling the total NC precursors volumetric flowrate were found to be necessary for prolonged flow stability imperative for continuous autonomous experimentation in flow. Following the high-temperature in-flow synthesis of NCs, the reactive phase droplets were rapidly cooled to the room temperature prior to entering the *in situ* characterization module to automatically acquire the absorption and PL spectra of the in-flow synthesized NCs. Additional details of the experimental setup can be found in the Experimental section.

Furthermore, an *in situ* characterization approach is crucial to accurately capture the absorption and PL spectra of the in-flow synthesized Cu-based MHP NCs for autonomous experimentation. Therefore, we validated the *in situ* obtained NC spectra achieved in the developed flow chemistry platform with *ex situ* measurement obtained by a benchtop spectrometer (FS5 spectrofluorometer, Edinburgh Instruments). Fig. S2† presents the benchmarking of *in situ vs. ex situ* absorption and PL spectra of the same Pb-free MHP NCs.

In this study, we focused on autonomous flow synthesis of a specific class of Pb-free MHP NCs, $Cs_3Cu_2I_5$ NCs. The goal of this study was not only to successfully synthesize $Cs_3Cu_2I_5$ NCs in flow but also rapidly discover the optimal synthetic route resulting in NCs with the highest PLQY. The emission peak intensity of $Cs_3Cu_2I_5$ NCs (PL_I) was utilized as a PLQY proxy in autonomous experimentation studies to achieve the most optimal $Cs_3Cu_2I_5$ NCs. Fig. S3† presents the linear correlation of *in situ* measured PL_I of the in-flow synthesized $Cs_3Cu_2I_5$ NCs *vs.* offline measured absolute PLQY (FS5 spectrofluorometer, Edinburgh Instruments).

A fully closed-loop autonomous experimentation requires a reliable process automation integrating experimental execution and data acquisition/analysis. The process automation workflow developed here enables complete control over the modular flow chemistry platform and is coupled with a Python script, which results in automatic experimental conditions parsing/execution and data acquisition/analysis to obtain the as-synthesized NCs spectral information in real-time. In addition, the custom-developed process automation code (LabVIEW) controls the fluid delivery module by directing the precursor solutions to the mixing and reaction module only once the system reaches a steady-state temperature. The process automation code also enables the automatic acquisition of absorption and PL spectra of the in-flow synthesized NCs when the equilibrium waiting time (t_E) is reached, which assures data being recorded once the NC synthesis reaches steady state. Detailed information regarding the developed process automation can be found in the ESI (see S4 and Fig. S4†).

Next, we studied the performance and reliability of the developed flow chemistry platform for continuous synthesis of $Cs_3Cu_2I_5$ NCs in flow. An ideal flow chemistry platform for autonomous experimentation should (i) ensure reliable continuous operation and (ii) result in successful and reproducible synthesis of colloidal NCs. These two metrics are important to benchmark the capabilities of the developed flow chemistry platform for the long-term continuous operation before delving into closed-loop autonomous experimentation. First, to assess the reliability of the developed flow chemistry platform for continuous synthesis of $Cs_3Cu_2I_5$ NCs, we analyzed three optical features obtained *in situ*: the absorbance value at the excitation wavelength of 300 nm ($Abs_{300\ nm}$ considered as a proxy for reaction yield), PL_I (considered as proxy for PLQY), and NCs emission peak area (PL_A). The response of the flow chemistry platform for all three optical features obtained *in situ* during continuous in-flow synthesis of $Cs_3Cu_2I_5$ NCs is illustrated in Fig. 3A. The overall experimental setup was found to reach steady state in 1.2× the total residence time (t_E = 1.2τ), where the total residence time is defined as the time it takes for the fluid to travel from the five-way fluidic connection used to form the CuI precursor stream to the *in situ* characterization module of the flow chemistry platform. After equilibrium is reached, $Abs_{300\ nm}$, PL_I, and PL_A showed standard deviations ~1.3%, ~1.1%, and ~1.0%, respectively. Then, we investigated the reproducibility of the flow chemistry platform for the in-flow synthesis of $Cs_3Cu_2I_5$ NCs. Specifically, an experimental perturbation study was conducted where a pre-selected reference condition was considered as the baseline, and a randomly selected synthesis condition was performed right after reaching steady state operation mode of each baseline synthesis condition. Fig. 3B presents the result of the reproducibility studies of the flow chemistry platform developed for autonomous synthesis of $Cs_3Cu_2I_5$ NCs with standard deviations of ~2.8%, ~1.2%, and ~1.1%, for $Abs_{300\ nm}$, PL_I, and PL_A, respectively, for the baseline condition after five replicates. The results shown in Fig. 3 prove the reliability of the flow chemistry platform shown in Fig. 2 for continuous synthesis of Pb-free MHP NCs with minimum

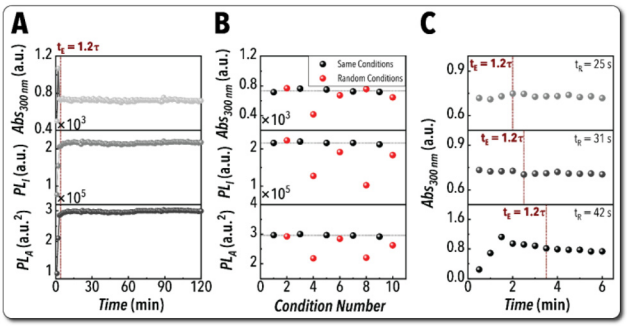

Fig. 3 Characterization of the developed flow chemistry platform performance for continuous operation and successful/reproducible synthesis of Pb-free MHP NCs: (A) Temporal evolution of $Abs_{300\ nm}$, PL_I, and PL_A for a specific synthesis condition over 120 min. (B) Assessment of the developed flow chemistry platform synthesis reproducibility by utilizing an experimental perturbation study. (C) Examination of the impact of dynamic residence time to determine the number of residence times (equilibrium time) applicable to all autonomous conditions.

experimental noise, that is considered a critical feature for minimizing the total optimization experimental cost of autonomous material synthesis labs.

In order to identify an appropriate equilibrium time needed to initiate the *in situ* characterization for all NC synthesis conditions during the autonomous experimentation campaigns, we conducted a dynamic residence time study of the in-flow synthesized $Cs_3Cu_2I_5$ NCs. The dynamic residence time study was performed to find how many residence times were needed for a given experimental condition to reach steady state operation. We tested three synthesis conditions in a sequence with varying residence times associated with three different reaction times (t_R), 25 s, 31 s, and 42 s, which were accommodated by modifying the total volumetric flowrate. Fig. 3C illustrates the values of $Abs_{300\ nm}$ for the three different reaction times tested. All three experimental conditions reached equilibrium in 1.2× the residence time ($t_E = 1.2\tau$), which is consistent with that of continuous operation investigation (Fig. 3A). The other *in situ* obtained optical features (PL_I and PL_A) for the three different reaction times tested here are illustrated in Fig. S5.† All three optical features showed a standard deviation below 5% once the equilibrium is reached.

The other important factor to ensure the reliability of the flow chemistry platform to continuously synthesize $Cs_3Cu_2I_5$ NCs is the proper mixing of the reactive phase within the droplets moving along the flow direction in the reaction module, that is controlled by the average flow velocity. Thus, we studied the effect of varying the total volumetric flowrate (and average flow velocity) on the NCs formation kinetics. A constant reaction time was implemented by adapting varying reaction tube length placed in the heating plate. As illustrated in Fig. 4A and B, the synthesis of $Cs_3Cu_2I_5$ NCs was observed to be mass transfer-limited at low flowrates. However, the optical properties of the in-flow synthesized $Cs_3Cu_2I_5$ NCs reached a plateau for NCs synthesized using the total volumetric flowrates higher than 600 μL min^{-1}, confirming the mass transfer-independency of the reaction at high mixings while utilizing the same reaction time. Next, we studied the effect of reaction time on the NCs formation kinetics. In order to ensure the reaction mixing-independency, a constant reaction tube length was placed in the heating plate, and different total flowrates above 600 μL min^{-1} were implemented to accommodate reaction times ranging from 25 s to 42 s. Fig. 4C and D show the effect of reaction time on the optical features of the in-flow synthesized $Cs_3Cu_2I_5$ NCs. While similar reaction yields were obtained for the tested reaction times, the NCs emission peak intensity was observed to drop slightly for the reaction times above ~28 s. The effects of shorter reaction times (<25 s) on the optical properties of the in-flow synthesized $Cs_3Cu_2I_5$ NCs is presented in Fig. S6.†

To better understand the synthesis chemical space of the $Cs_3Cu_2I_5$ NCs, we performed a partial grid search on the input synthesis parameters while maintaining the reaction time constant using the automated operation mode of the developed flow chemistry platform. Specifically, the parameter space was explored by varying only one input parameter of interest while maintaining the other parameters constant. The *in situ* PL and absorption spectra associated with this parameter space exploration are illustrated in Fig. 5 and S7,† respectively. The partial gird search findings glean valuable insights into the formation mechanism of the Cu-based MHP NCs at high temperatures and facilitate adjusting the parameter space boundaries *via* dimensionless equations, which ensures an efficient closed-loop autonomous experimentation by reducing the total experimental time and material consumption. More details regarding dimensionless equations can be found in ESI (see S8†). As illustrated in Fig. 5, the peak emission wavelength of $Cs_3Cu_2I_5$ NCs (450 nm) is independent of the input synthesis parameters, which is attributed to the STE emission mechanism of Cu-based MHP NCs. By increasing [Cs-oleate], the secondary peak at the wavelength of ~380 nm increases, which is potentially due to the presence of excess OA ligand used to make Cs-oleate soluble at room temperature (Fig. 5A). However, there is no consistent trend for the reaction yield and PL_I of $Cs_3Cu_2I_5$ NCs (Fig. 5A and S7A†). This is consistent with Li *et al.* observation where an increase in the Cs-oleate : CuI ratio does not necessarily increase the quality of the synthesized NCs.[25] Both NCs reaction yield and PL_I were seen to increase by increasing the [CuI], as it facilitates the formation of $Cs_3Cu_2I_5$ NCs (Fig. 5B and S7B†). Increasing the concentration of OA associated with both Cs-oleate and CuI precursor streams elevates the NCs reaction yield, as it could potentially bring more freely available Cs^+ and Cu^+ ions into the crystalline structure, respectively (Fig. S7C and S7D†). However, the trend observed for the effects of OA concentration on the NCs PL_I suggests an optimal value for this input parameter (Fig. 5C and D). Increasing the [OAm] associated

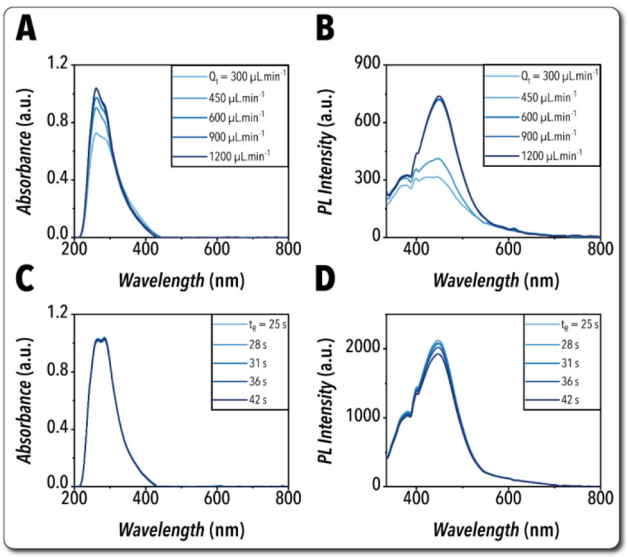

Fig. 4 In-flow screening for: the effect of total volumetric flowrate on the *in situ* recorded (A) absorption and (B) PL spectra while utilizing the same reaction time. The effect of reaction time on the *in situ* recorded (C) absorption and (D) PL spectra while utilizing total flowrates above 600 μL min^{-1} to ensure the reaction mixing-independency.

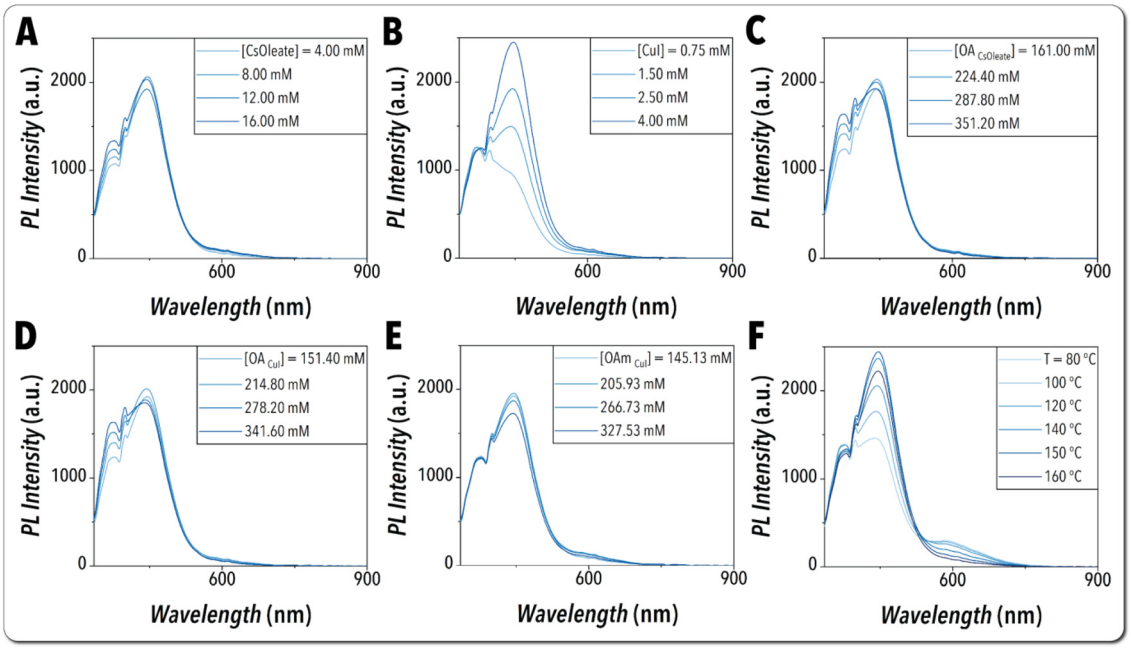

Fig. 5 *In situ* recorded UV-Vis PL spectra of the partial grid search on the input synthesis parameters, including (A) [CsOleate], (B) [CuI], (C) [$OA_{CsOleate}$], (D) [OA_{CuI}], (E) [OAm_{CuI}], and (F) reaction temperature, while maintaining the reaction time constant. The complete list of experimental conditions used for the partial grid search study is provided in Table S1.†

with the CuI precursor stream also enhances the overall reaction yield, as OAm ions could form complexes with and bring more halide ions into the crystalline structure (Fig. S7E†). However, the $Cs_3Cu_2I_5$ NCs PL_I decreases while increasing the concentration of OAm, which is potentially due to the detrimental effects of excess OAm that could deteriorate the crystalline integrity and cause NCs decomposition (Fig. 5E). The effects of reaction temperature on the optical properties of $Cs_3Cu_2I_5$ NCs were also investigated. The secondary PL emission peak at the wavelength of ~600 nm suggests a secondary NC population, observed at lower reaction temperatures (<120 °C). Increasing the reaction temperature to 150 °C, enhances PL_I of $Cs_3Cu_2I_5$ NCs with the peak emission wavelength of 450 nm. However, increasing the reaction temperature beyond 150 °C lowered PL_I compared to lower temperatures, which can potentially be attributed to the NCs decomposition at higher temperatures (Fig. 5F). Considering these initial screening results, the temperature range of 120 °C–150 °C was utilized for subsequent autonomous synthesis science studies of $Cs_3Cu_2I_5$ NCs.

The high-dimensional chemical space of Pb-free MHP NCs brings significant challenges while searching for the optimal synthesis condition required to produce $Cs_3Cu_2I_5$ NCs with enhanced optical properties. The time- and resource-intensive high-throughput combinatorial screening not only requires experts' intervention but could also only navigate around a local experimental space optimum. The closed-loop autonomous experimentation mode, on the other hand, offers a more informed chemical space exploration strategy with minimum experimental iterations (cost). Herein, we developed an informed BO strategy and integrated it with the automated flow chemistry platform to rapidly map the experimental synthesis space of Pb-free MHP NCs for two applications (i) build a digital twin model and (ii) autonomous optical property optimization of the in-flow synthesized Pb-free MHP NCs. The closed-loop nature of the developed SDFL enables accelerated NC synthesis space exploration *via* automatic learning/acquiring new experimental data with continuously improved ML model prediction accuracy. The autonomous experimental campaigns using BO perform the following automated steps in an iterative manner: (i) surrogate model initialization, (ii) selection of the next set of experiment(s) using a specific decision policy (reaction space exploration or exploitation), (iii) conduction of the machine-selected experiment(s) in the microfluidic platform, (iv) *in situ* data acquisition/analysis, and (v) retraining the surrogate model using the updated experimental dataset.

In our prior ML benchmarking studies, ensemble neural network (ENN) was found to outperform other ML strategies for autonomous material synthesis in flow.[58,59] Thus, we utilized ENN to construct surrogate predictive models of the developed SDFL. To build the surrogate model of the in-flow synthesis of Cu-based MHP NCs, we considered seven nondimensionalized synthesis input parameters (X_i, i = 1–7), *i.e.*, ML model features, including reaction temperature and volumetric flowrates of CuI, Cs-oleate, two OA-ODE streams, OAm-ODE, and solvent (ODE) associated with the CuI stream, as well as one output parameter (PL_I).

The digital twin experimental campaign started with surrogate model initialization. This initialization step included nine

initial experimental conditions selected by the latin hypercube sampling (LHS) method passed to the flow chemistry platform for automatic experimentation to build the initial dataset needed to initialize the BO surrogate model. Next, we implemented a fully explorative BO experimental campaign to autonomously generate high-quality experimental data required for building a digital twin model of the in-flow Pb-free MHP NC synthesis. The parameter space mapping for the digital twin model construction was conducted using the maximum variance (MV) decision policy, which is based upon uncertainty quantification. Further details of the MV-based autonomous experimental campaign can be found in the ESI (see S8†). The goal of the MV campaign was to identify the minimum number of experiments required to build an accurate digital twin model both for fundamental studies of the Pb-free MHP NC synthesis in the flow reactor and to be used as the knowledge transfer (informed surrogate model) for subsequent optimization campaigns.

Fig. 6 presents a summary of the explorative BO campaigns for building a digital twin model of Pb-free MHP NCs synthesized in the developed flow chemistry platform. *R*-Squared (R^2) of the mean ENN-predicted *vs.* the experimentally measured output parameter, PL_I, was used to evaluate the digital twin model performance. A model accuracy of 80% for the test dataset was considered as the threshold criterion to identify the optimal ENN structure. The digital twin model with an acceptable prediction accuracy ~81% was achieved after 51 autonomous explorative experimental iterations.

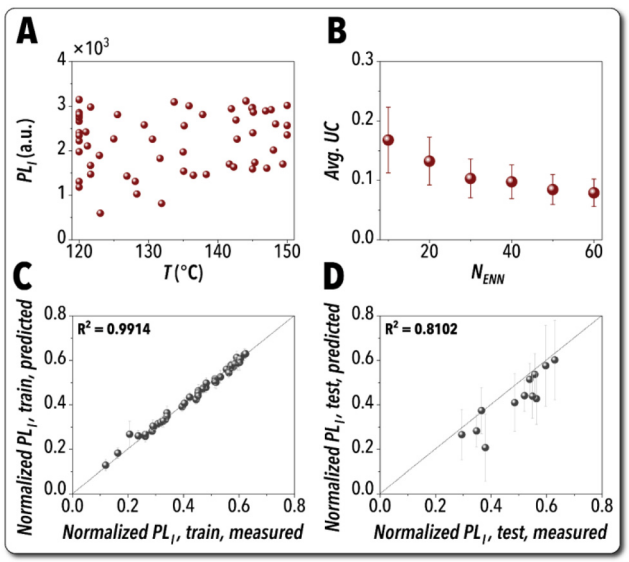

Fig. 6 Development of the digital twin model: (A) Experimentally measured PL_I values *vs.* the input parameter temperature for all 60 data points achieved from LHS and MV-based explorative campaign. (B) Average uncertainties and corresponding standard deviations obtained from applying the ENN models, trained using different dataset sizes, on an independent dataset drawn from MC sampler. Digital twin accuracy plots for (C) training and (D) test sets using an 80/20 split ratio. A complete list of autonomous experiments for digital twin model training is provided in Table S2.†

Fig. 6A shows the experimentally measured PL_I values *vs.* the input parameter temperature for all 60 data points including 9 achieved from LHS and 51 achieved from the MV-based explorative campaign. In order to assess the effect of training dataset size on the accuracy and performance of the trained digital twin model, we tested each ENN model trained on datasets with various dataset sizes (10–60 data points) on an independent set of 1000 input conditions, each including seven dimensionless input parameters, drawn from a Monte Carlo (MC) sampler. The average and standard deviation of each digital twin model's uncertainty trained with different dataset sizes are shown in Fig. 6B. The ENN model trained on 60 experimental data points resulted in the lowest average uncertainty on the MC-sampled datapoints. The digital twin prediction accuracy plots for the ENN model trained with the 60 autonomously generated experimental data points (LHS + MV campaign) are presented in Fig. 6C and D for the training and test sets, respectively.

Next, we utilized the trained digital twin model to better understand the underlying mechanism of $Cs_3Cu_2I_5$ NCs synthetic chemistry. A robust digital twin with a high prediction accuracy can be utilized to rapidly identify the key synthesis parameters controlling the material properties (PL_I of Pb-free MHP NCs). Shapley analysis technique[60] enables investigating the relative importance of each independent ML model feature (*i.e.*, NCs synthesis parameter) on tuning the model output (PL_I). The Shapley analysis ranks the ML model features from the most to the least effective. The data points shown in the Shapley analysis plot for each model feature represents an individual experimental data generated by the SDFL. A model feature has a positive effect on the output if the corresponding data points on a Shapley analysis plot move towards positive SHAP values. The Shapley explanation plots obtained from the digital twin model of $Cs_3Cu_2I_5$ NCs is illustrated in Fig. 7A. Based on the Shapley analysis results, the CuI precursor concentration and reaction temperature were identified as the most important synthesis input parameters affecting the *in situ* optical feature of interest (PL_I). Based on the SHAP values distributions, the NCs PL_I is elevated as the CuI concen-

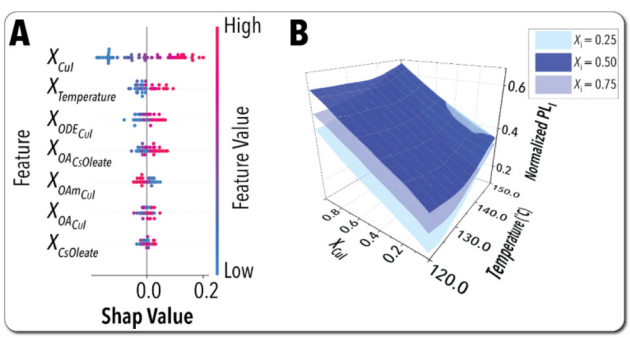

Fig. 7 Accelerated fundamental studies of $Cs_3Cu_2I_5$ NCs synthetic chemistry using the digital twin model: (A) Shapley additive explanation plot of PL_I. (B) Surface plot showing the impact of the top two synthesis input parameters on PL_I.

tration increases. Excess CuI provides a Cu-oleate-rich reaction environment, enhancing the $Cs_3Cu_2I_5$ NC formation.[61] A higher reaction temperature is also found to result in a higher PL_I value. As reported previously, decreasing the average size of $Cs_3Cu_2I_5$ NCs has a diminishing effect on their PLQY. The direct relationship between the NC size and PLQY of Cu-based MHP NCs may be attributed to the increased surface defects and non-radiative recombination that originates from the larger specific surface area of smaller $Cs_3Cu_2I_5$ NCs. It has been previously reported that increasing reaction temperature results in formation of larger $Cs_3Cu_2I_5$ NCs with higher PLQY.[62] This finding is in agreement with the SDFL results where the $Cs_3Cu_2I_5$ NCs synthesized at higher reaction temperatures resulted in higher PL_I values, corresponding to higher PLQYs. This finding was further validated by transmission electron microscopy (TEM) imaging where two $Cs_3Cu_2I_5$ NC samples were synthesized in the microfluidic platform at two different reaction temperatures (130 °C and 150 °C) at fixed values of other synthesis input parameters. The higher reaction temperature was found to not only improve the NCs morphology uniformity but also increase the NCs average size (see Fig. S8†). Additionally, within the reaction time range used in autonomous campaigns (25 s–42 s), prolonged reaction times were found to diminish the quality of the in-flow synthesized $Cs_3Cu_2I_5$ NCs, which is potentially attributed to the NC decomposition. In addition, increasing the concentration of OA associated with both Cs-oleate and CuI precursor streams was revealed to enhance PL_I of $Cs_3Cu_2I_5$ NCs, which illustrates the crucial passivating role of OA in enhancing the PL emission of NCs by reducing nonradiative recombination.[25] Increasing the concentration of OAm associated with the CuI precursor stream was found to have a diminishing impact on PL_I of $Cs_3Cu_2I_5$ NCs, potentially due to the detrimental effects of excess OAm on the NC growth.[63,64] It is worth noting that the concentration of the Cs-oleate precursor was not ranked as highly important in controlling PL_I of $Cs_3Cu_2I_5$ NCs, which suggests the initial concentration of the Cs-oleate precursor solution in this study was relatively high.

In addition to facilitating the NC synthesis process analysis, the digital twin model obtained *via* the explorative autonomous campaign can be utilized to visualize the high-dimensional chemical space of the Pb-free MHP NCs. Fig. 7B illustrates the visualization of the output (PL_I) surface plot as a function of the two most important model features (synthesis input parameters) obtained from the Shapley analysis while maintaining the remaining synthesis parameters constant. As observed, the $Cs_3Cu_2I_5$ NCs PL_I is improved as the CuI precursor concentration and the reaction temperature increase, which agrees well with what we discussed above.

In the subsequent autonomous experimentation campaigns, we utilized the trained digital twin as the surrogate model in a BO framework for autonomous emission optimization of the in-flow synthesized Pb-free MHP NCs. Utilization of the trained digital twin enables access to the prior knowledge obtained in the autonomous explorative campaign to accelerate discovery of the optimal synthetic route of the highest-performing $Cs_3Cu_2I_5$ NCs with minimal experimental cost (number of experimental iterations). The automated experiment-selection strategy of BO has a profound impact on the navigation through the accessible experimental synthesis space of Pb-free MHP NCs. Thus, we explored three different decision-making policies, expected improvement (EI), pure exploitation (EPLT), and upper confidence bound (UCB), and benchmarked them against a random sampling campaign. An experimental budget of 10 iterations was utilized for each autonomous NC synthesis optimization campaign. Details of different optimization campaigns are reported in the ESI (see S8†). Fig. 8A presents the results of autonomous NC synthesis optimization campaigns conducted with the same batch of NC precursors over 1 day of continuous experimentation with no manual intervention. All three decision-making policies (EI, EPLT, and UCB) were successful in identifying $Cs_3Cu_2I_5$ NC synthetic routes with PL_I values exceeding the maximum value achieved in both partial grid search and explorative campaign. This result highlights the necessity of informed chemical space exploration to identify the synthetic route of highest-performing $Cs_3Cu_2I_5$ NCs. The EI experiment-selection policy using the informed surrogate model (trained on 60 experiments among which 51 were autonomously selected) reached the maximum PL_I within the least number of experimental iterations (six experiments), while UCB and EPLT policies required eight and ten iterations, respectively, to identify the highest-performing $Cs_3Cu_2I_5$ NCs. On the other hand, the random sampling campaign significantly underperformed within the same experimental budget with the maximum PL_I ~20% lower than the best value identified by the EI decision-making policy. This result further demonstrates the importance of active learning for accelerated navigation and optimization of high-dimensional synthesis spaces. The EI decision-making policy directly measures the improvement of the defined objective function and emphasizes the actions with the highest expected improvement over the current best value in the dataset, allowing for faster convergence to the optimal conditions compared to the other decision-making policies tested here. Fig. 8B illustrates the evolution of independent input parameter selections of different decision-making policies within the given experimental budget. It should be pointed out that the uncertainty of the digital twin model necessitates the closed-loop autonomous experimental optimization campaigns to identify the optimal synthetic routes while continuously updating and improving the current belief (surrogate model).

Fig. 8C shows the *in situ* absorption and PL spectra of the highest-performing $Cs_3Cu_2I_5$ NCs autonomously discovered using an informed BO framework with an EI decision-making policy. The in-flow synthesized $Cs_3Cu_2I_5$ NCs (purified) had a PLQY of ~17%. Fig. 8D illustrates the X-ray diffraction (XRD) analysis of the purified high-performing $Cs_3Cu_2I_5$ NCs synthesized in-flow, obtained using the EI decision-making policy. The XRD data confirms an orthorhombic crystal structure of $Cs_3Cu_2I_5$ NCs.[65] Fig. S9† presents a TEM image of the highest-performing $Cs_3Cu_2I_5$ NCs autonomously achieved

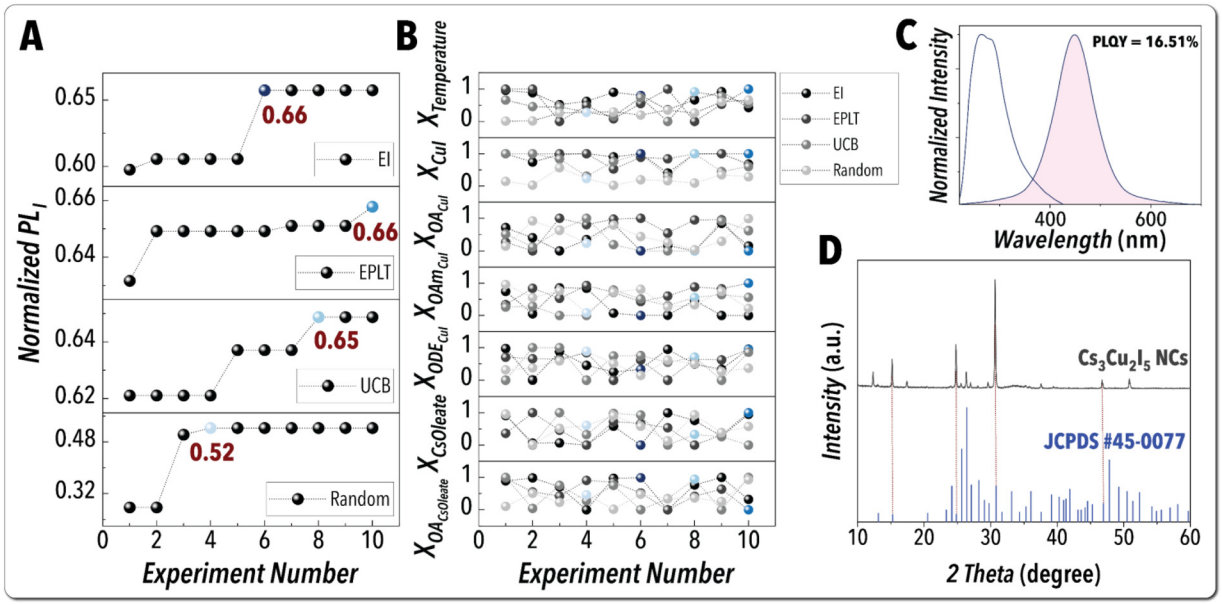

Fig. 8 Closed-loop autonomous optimization campaigns: (A) Representation of the best-condition-so-far and (B) Evolution of independent input parameter selections for autonomous search of finding the highest PL_I in optimization campaigns under different decision-making policies, benchmarked against random sampling. (C) The *in situ* absorption and PL spectra and (D) XRD pattern of the highest-performing $Cs_3Cu_2I_5$ NCs discovered using the EI experiment-selection policy. A complete list of autonomous experiments is provided in Table S3.†

using an EI decision policy. Additional details of the purification protocol, TEM imaging, and XRD analysis are reported in the ESI (see S9†).

4. Conclusions

In summary, we have developed an autonomous experimentation platform for accelerated synthesis science studies and synthetic route optimization of Pb-free MHP NCs. The developed modular microfluidic platform, for the first time, enabled successful and reproducible synthesis of a particular type of Pb-free MHPs, $Cs_3Cu_2I_5$ NCs, in flow. The automated operation mode of the developed flow chemistry platform was utilized to rapidly investigate the effects of synthesis input parameters on the optical properties of $Cs_3Cu_2I_5$ NCs. The SDFL equipped with a BO framework was then deployed to rapidly map the synthesis-property space of $Cs_3Cu_2I_5$ NCs. The autonomously mapped NC synthesis space was then utilized for (i) building a predictive digital twin model and (ii) closed-loop optimization of the optical properties of the in-flow synthesized Pb-free MHP NCs. The developed digital twin model was first utilized for fundamental mechanistic studies of the Cu-based MHP NCs. Next, the digital twin model was used as an informed surrogate model for fast-tracked synthetic route discovery of high-performing $Cs_3Cu_2I_5$ NCs with minimum chemical consumption and waste generation. The SDFL unveiled in this work can accelerate the development and adoption of eco-friendly MHP NCs by printed clean energy technologies.

Author contributions

S. S. and F. B. contributed equally to this work. M. A., T. K., and D. Y. S. conceived the project. S. S., J. A. B., N. O., T. D. C., R. A., J. X., K. G. R., and M. A. designed the algorithms. S. S. programmed the digital twin and Bayesian Optimization algorithms and analyzed all experimental data. F. B. designed and built the flow chemistry platform with S. S. F. B. designed and implemented the process automation module of the self-driving fluidic lab with J. A. B. S. S. and F. B. conducted the partial grid search and autonomous nanocrystal synthesis campaigns. H. D., V. S. P., and C. S. helped with the precursor chemistry development. F. D., J. X., and N. M. helped with the analysis and development of Fig. 1. M. A. acquired funding and directed the project. S. S., F. B., and M. A. drafted the manuscript. All authors provided feedback on the manuscript.

Conflicts of interest

The authors declare no conflict of interest.

Acknowledgements

The authors acknowledge the financial support from Samsung Advanced Institute of Technology. This work was performed in part at the Analytical Instrumentation Facility (AIF) at North Carolina State University, which is supported by the State of North Carolina and the National Science Foundation (award number ECCS-1542015). The AIF is a member of the

North Carolina Research Triangle Nanotechnology Network (RTNN), a site in the National Nanotechnology Coordinated Infrastructure (NNCI).

References

1 M. V. Kovalenko, L. Protesescu and M. I. Bodnarchuk, *Science*, 2017, **358**, 745–750.
2 A. F. Gualdrón-Reyes, S. Masi and I. Mora-Seró, *Trends Chem.*, 2021, **3**, 499–511.
3 Y. Zhang, T. D. Siegler, C. J. Thomas, M. K. Abney, T. Shah, A. De Gorostiza, R. M. Greene and B. A. Korgel, *Chem. Mater.*, 2020, **32**, 5410–5423.
4 K. Abdel-Latif, F. Bateni, S. Crouse and M. Abolhasani, *Matter*, 2020, **3**, 1053–1086.
5 Y. Bai, M. Hao, S. Ding, P. Chen and L. Wang, *Adv. Mater.*, 2022, **34**, 2105958.
6 A. Pan, B. He, X. Fan, Z. Liu, J. J. Urban, A. P. Alivisatos, L. He and Y. Liu, *ACS Nano*, 2016, **10**, 7943–7954.
7 S. Yakunin, L. Protesescu, F. Krieg, M. I. Bodnarchuk, G. Nedelcu, M. Humer, G. De Luca, M. Fiebig, W. Heiss and M. V. Kovalenko, *Nat. Commun.*, 2015, **6**, 8056.
8 P. Ramasamy, D.-H. Lim, B. Kim, S.-H. Lee, M.-S. Lee and J.-S. Lee, *Chem. Commun.*, 2016, **52**, 2067–2070.
9 V. I. Klimov, T. A. Baker, J. Lim, K. A. Velizhanin and H. McDaniel, *ACS Photonics*, 2016, **3**, 1138–1148.
10 T. C. Jellicoe, J. M. Richter, H. F. J. Glass, M. Tabachnyk, R. Brady, S. E. Dutton, A. Rao, R. H. Friend, D. Credgington, N. C. Greenham and M. L. Böhm, *J. Am. Chem. Soc.*, 2016, **138**, 2941–2944.
11 A. B. Wong, Y. Bekenstein, J. Kang, C. S. Kley, D. Kim, N. A. Gibson, D. Zhang, Y. Yu, S. R. Leone, L.-W. Wang, A. P. Alivisatos and P. Yang, *Nano Lett.*, 2018, **18**, 2060–2066.
12 X. Wu, W. Song, Q. Li, X. Zhao, D. He and Z. Quan, *Chem. – Asian J.*, 2018, **13**, 1654–1659.
13 Y. Wei, K. Li, Z. Cheng, M. Liu, H. Xiao, P. Dang, S. Liang, Z. Wu, H. Lian and J. Lin, *Adv. Mater.*, 2019, **31**, 1807592.
14 X. Lü, Y. Wang, C. C. Stoumpos, Q. Hu, X. Guo, H. Chen, L. Yang, J. S. Smith, W. Yang, Y. Zhao, H. Xu, M. G. Kanatzidis and Q. Jia, *Adv. Mater.*, 2016, **28**, 8663–8668.
15 L. Zhou, Y.-F. Xu, B.-X. Chen, D.-B. Kuang and C.-Y. Su, *Small*, 2018, **14**, 1703762.
16 B. Yang, J. Chen, S. Yang, F. Hong, L. Sun, P. Han, T. Pullerits, W. Deng and K. Han, *Angew. Chem.*, 2018, **130**, 5457–5461.
17 B. Yang, F. Hong, J. Chen, Y. Tang, L. Yang, Y. Sang, X. Xia, J. Guo, H. He, S. Yang, W. Deng and K. Han, *Angew. Chem.*, 2019, **131**, 2300–2305.
18 F. Locardi, M. Cirignano, D. Baranov, Z. Dang, M. Prato, F. Drago, M. Ferretti, V. Pinchetti, M. Fanciulli, S. Brovelli, L. De Trizio and L. Manna, *J. Am. Chem. Soc.*, 2018, **140**, 12989–12995.
19 Z. Luo, Q. Li, L. Zhang, X. Wu, L. Tan, C. Zou, Y. Liu and Z. Quan, *Small*, 2020, **16**, 1905226.
20 S. Seth and A. Samanta, *J. Phys. Chem. Lett.*, 2018, **9**, 176–183.
21 C. Zhou, H. Lin, Q. He, L. Xu, M. Worku, M. Chaaban, S. Lee, X. Shi, M.-H. Du and B. Ma, *Mater. Sci. Eng., R*, 2019, **137**, 38–65.
22 H. Lin, C. Zhou, Y. Tian, T. Siegrist and B. Ma, *ACS Energy Lett.*, 2018, **3**, 54–62.
23 M. D. Smith, B. A. Connor and H. I. Karunadasa, *Chem. Rev.*, 2019, **119**, 3104–3139.
24 S. Li, J. Luo, J. Liu and J. Tang, *J. Phys. Chem. Lett.*, 2019, **10**, 1999–2007.
25 Y. Li, P. Vashishtha, Z. Zhou, Z. Li, S. B. Shivarudraiah, C. Ma, J. Liu, K. S. Wong, H. Su and J. E. Halpert, *Chem. Mater.*, 2020, **32**, 5515–5524.
26 Y. Lu, S. Fang, G. Li and L. Li, *J. Alloys Compd.*, 2022, **903**, 163924.
27 Z. S. Campbell, F. Bateni, A. A. Volk, K. Abdel-Latif and M. Abolhasani, *Part. Part. Syst. Charact.*, 2020, **37**, 2000256.
28 A. A. Volk, R. W. Epps and M. Abolhasani, *Adv. Mater.*, 2021, **33**, 2004495.
29 A. Vikram, A. Zahid, S. S. Bhargava, H. Jang, A. Sutrisno, A. Khare, P. Trefonas, M. Shim and P. J. A. Kenis, *ACS Appl. Nano Mater.*, 2020, **3**, 12325–12333.
30 I. Shestopalov, J. D. Tice and R. F. Ismagilov, *Lab Chip*, 2004, **4**, 316.
31 B. K. H. Yen, A. Günther, M. A. Schmidt, K. F. Jensen and M. G. Bawendi, *Angew. Chem.*, 2005, **117**, 5583–5587.
32 V. Sebastian Cabeza, S. Kuhn, A. A. Kulkarni and K. F. Jensen, *Langmuir*, 2012, **28**, 7007–7013.
33 M. Abolhasani, C. W. Coley, L. Xie, O. Chen, M. G. Bawendi and K. F. Jensen, *Chem. Mater.*, 2015, **27**, 6131–6138.
34 Y. Gao, B. Pinho and L. Torrente-Murciano, *Curr. Opin. Chem. Eng.*, 2020, **29**, 26–33.
35 J. Sui, J. Yan, D. Liu, K. Wang and G. Luo, *Small*, 2020, **16**, 1902828.
36 F. Bateni, R. W. Epps, K. Abdel-latif, R. Dargis, S. Han, A. A. Volk, M. Ramezani, T. Cai, O. Chen and M. Abolhasani, *Matter*, 2021, **4**, 2429–2447.
37 K. Antami, F. Bateni, M. Ramezani, C. E. Hauke, F. N. Castellano and M. Abolhasani, *Adv. Funct. Mater.*, 2022, **32**, 2108687.
38 M. O. Besenhard, S. Pal, L. Storozhuk, S. Dawes, N. T. K. Thanh, L. Norfolk, S. Staniland and A. Gavriilidis, *Lab Chip*, 2023, **23**, 115–124.
39 R. W. Epps, F. Delgado-Licona, H. Yang, T. Kim, A. A. Volk, S. Han, S. Jun and M. Abolhasani, *Adv. Mater. Technol.*, 2023, **8**, 2201845.
40 R. W. Epps, A. A. Volk, M. Y. S. Ibrahim and M. Abolhasani, *Chem*, 2021, **7**, 2541–2545.
41 A. A. Volk, Z. S. Campbell, M. Y. S. Ibrahim, J. A. Bennett and M. Abolhasani, *Annu. Rev. Chem. Biomol. Eng.*, 2022, **13**, 45–72.
42 K. F. Jensen, *AIChE J.*, 2017, **63**, 858–869.
43 M. Abolhasani, K. A. Brown and Guest Editors, *MRS Bull.*, 2023, **48**, 134–141.

44 M. Abolhasani and E. Kumacheva, *Nat. Synth.*, 2023, **2**, 483–492.
45 C. W. Coley, N. S. Eyke and K. F. Jensen, *Angew. Chem., Int. Ed.*, 2020, **59**, 22858–22893.
46 A. Vikram, K. Brudnak, A. Zahid, M. Shim and P. J. A. Kenis, *Nanoscale*, 2021, **13**, 17028–17039.
47 M. Krenn, R. Pollice, S. Y. Guo, M. Aldeghi, A. Cervera-Lierta, P. Friederich, G. dos Passos Gomes, F. Häse, A. Jinich, A. Nigam, Z. Yao and A. Aspuru-Guzik, *Nat. Rev. Phys.*, 2022, **4**, 761–769.
48 H. Lv and X. Chen, *Nanoscale*, 2022, **14**, 6688–6708.
49 Z. Tu, T. Stuyver and C. W. Coley, *Chem. Sci.*, 2023, **14**, 226–244.
50 Z. Yao, Y. Lum, A. Johnston, L. M. Mejia-Mendoza, X. Zhou, Y. Wen, A. Aspuru-Guzik, E. H. Sargent and Z. W. Seh, *Nat. Rev. Mater.*, 2022, **8**, 202–215.
51 C. J. Taylor, K. C. Felton, D. Wigh, M. I. Jeraal, R. Grainger, G. Chessari, C. N. Johnson and A. A. Lapkin, *ACS Cent. Sci.*, 2023, **9**, 957–968.
52 A. M. Schweidtmann, A. D. Clayton, N. Holmes, E. Bradford, R. A. Bourne and A. A. Lapkin, *Chem. Eng. J.*, 2018, **352**, 277–282.
53 A. D. Clayton, A. M. Schweidtmann, G. Clemens, J. A. Manson, C. J. Taylor, C. G. Niño, T. W. Chamberlain, N. Kapur, A. J. Blacker, A. A. Lapkin and R. A. Bourne, *Chem. Eng. J.*, 2020, **384**, 123340.
54 A. D. Clayton, J. A. Manson, C. J. Taylor, T. W. Chamberlain, B. A. Taylor, G. Clemens and R. A. Bourne, *React. Chem. Eng.*, 2019, **4**, 1545–1554.
55 H. Tao, T. Wu, S. Kheiri, M. Aldeghi, A. Aspuru-Guzik and E. Kumacheva, *Adv. Funct. Mater.*, 2021, **31**, 2106725.
56 A. A. Volk, R. W. Epps, D. T. Yonemoto, B. S. Masters, F. N. Castellano, K. G. Reyes and M. Abolhasani, *Nat. Commun.*, 2023, **14**, 1403.
57 C. Lu, M. W. Wright, X. Ma, H. Li, D. S. Itanze, J. A. Carter, C. A. Hewitt, G. L. Donati, D. L. Carroll, P. M. Lundin and S. M. Geyer, *Chem. Mater.*, 2019, **31**, 62–67.
58 R. W. Epps, M. S. Bowen, A. A. Volk, K. Abdel-Latif, S. Han, K. G. Reyes, A. Amassian and M. Abolhasani, *Adv. Mater.*, 2020, **32**, 2001626.
59 R. W. Epps, A. A. Volk, K. G. Reyes and M. Abolhasani, *Chem. Sci.*, 2021, **12**, 6025–6036.
60 S. M. Lundberg and S. I. Lee, A unified approach to interpreting model predictions, in *Proceedings of the Advances in Neural Information Processing Systems*, Long Beach, CA, USA, 2017, pp. 4765–4774.
61 C.-X. Li, S.-B. Cho, D.-H. Kim and I.-K. Park, *Chem. Mater.*, 2022, **34**, 6921–6932.
62 J. Chen, Y. Li, Z. Yin, S. Wang, O. Lin, W. Niu, F. Teng and A. Tang, *J. Mater. Chem. C*, 2023, **11**, 13030–13038.
63 E. Yassitepe, Z. Yang, O. Voznyy, Y. Kim, G. Walters, J. A. Castañeda, P. Kanjanaboos, M. Yuan, X. Gong, F. Fan, J. Pan, S. Hoogland, R. Comin, O. M. Bakr, L. A. Padilha, A. F. Nogueira and E. H. Sargent, *Adv. Funct. Mater.*, 2016, **26**, 8757–8763.
64 N. C. Anderson, M. P. Hendricks, J. J. Choi and J. S. Owen, *J. Am. Chem. Soc.*, 2013, **135**, 18536–18548.
65 T. Jun, K. Sim, S. Iimura, M. Sasase, H. Kamioka, J. Kim and H. Hosono, *Adv. Mater.*, 2018, **30**, 1804547.
66 F. Bateni, S. Sadeghi, N. Orouji, J. A. Bennett, V. S. Punati, C. Stark, J. Wang, M. C. Rosko, O. Chen, F. N. Castellano, K. G. Reyes and M. Abolhasani, *Adv. Energy Mater.*, 2023, 2302303.